Advanced Materials

ADVANCED MATERIALS
www.advmat.de

RESEARCH ARTICLE

Microphase-Separated Elastomers Enable Synergistic Dispersion and Coalescence Control in Conductive Pastes for Fine Printing

Zhizhuo Hou[1] | Haocheng Ji[2] | Zhaohuang Zhan[1] | Jian Liu[1] | Luyi Yang[1] | Yuan Lin[3] | Feng Pan[1]

[1]School of Advanced Materials, Peking University Shenzhen Graduate School, Peking University, Shenzhen, China | [2]Tsinghua-Berkeley Shenzhen Institute & Tsinghua Shenzhen International Graduate School, Tsinghua University, Shenzhen, China | [3]Key Laboratory of Photochemistry, Institute of Chemistry, Chinese Academy of Sciences, Beijing, China

Correspondence: Luyi Yang (yangly@pkusz.edu.cn) | Yuan Lin (linyuan@iccas.ac.cn) | Feng Pan (panfeng@pkusz.edu.cn)

Received: 14 October 2025 | **Revised:** 24 February 2026 | **Accepted:** 5 March 2026

Keywords: conductive paste | microphase separation | printable electronics | rheological property | sintering behavior

ABSTRACT

With the advancement of high-power and fine-feature electronic devices, metallic pastes have emerged as essential conductive materials, whose performance largely depends on the structure of the organic carrier. Conventional polyamide wax thixotropic agents, based on amide hydrogen-bonded networks, are often overly rigid, leading to poor leveling after demolding and local aggregation or porosity under high silver loadings. To overcome these limitations, this study introduces a microphase-separated styrene-ethylene-propylene-styrene (SEPS) block copolymer as a thixotropic agent. Through the synergy between hard and soft segments, SEPS forms a reversible microgel network that enhances organic-inorganic interfacial interactions and metal particle dispersion. The hard segments interact with particle surfaces to improve dispersion, while soft segments enable shear-thinning and rapid viscoelastic recovery, thereby achieving high-resolution, fine-line printing. Moreover, during thermal treatment, the stepwise decomposition of the organic phase promotes silver particle necking and grain growth, further densifying the electrode. Consequently, a low porosity (8.66%) and uniform electrode morphology are achieved, resulting in an extremely low resistivity (3.03 μΩ·cm). Through synergistic control of rheology and particle coalescence, this work provides a strategy for optimizing metallic functional pastes toward precision-printed electronic devices.

1 | Introduction

As electronic devices advance toward microstructuring and large-scale production, especially in printed electronics and photovoltaic cells, high-precision and reliable printed electrodes have become critical for device performance and yield [1–3]. The demand for such electrodes highlights the importance of functional conductive pastes. Their key properties, including rheology and electrical conductivity, are primarily determined by multiscale interfacial interactions between the organic carrier and conductive fillers [4, 5]. Conductive particles must remain uniformly dispersed during storage and printing, and must coalesce and grow during drying and thermal treatment to form a denser conductive network.

As a typical functional conductive paste, silver pastes consist of inorganic silver powders and organic carriers (including thixotropic agents, solvents, and rheology modifiers), whose interplay governs both the microscopic evolution and the macroscopic performance during printing and sintering [6–10]. The organic carrier not only provides a liquid-phase scaffold for dispersion stability at high solid content but also modulates particle

interactions and interfaces through wetting, adsorption, and network reconstruction. Consequently, to meet the increasing demands for finer lines, faster printing, and higher throughput, the paste must exhibit proper flow behavior for screen printing, including appropriate yield stress, shear-thinning behavior, and thixotropic recovery [11–13]. These rheological parameters control the paste's printability and pattern fidelity, which in turn affect the resulting microstructure and electrical performance [14, 15].

In recent years, significant progress has focused on tuning the organic carrier components to improve the macroscopic performance of silver pastes, with particular attention to enhancing rheology, particle dispersion, and printability [16–20]. Notably, Kuzina et al. showed that the properties of organic gel structures can be precisely controlled through compositional adjustments, highlighting the potential of carrier design [21]. Although previous studies have advanced silver paste performance through optimization of formulations and processing parameters, systematic and mechanistic studies on the interfacial chemistry and micro-scale interactions between the organic carrier and silver particles are still lacking.

Thixotropic and thickening agents are essential components of the organic carrier, forming a structural framework through polymer chain entanglement and physical networks. Within this framework, silver particles are dispersed and partially associate with network nodes, resulting in a more stable internal structure. Polyamide wax (PW), due to its amide groups, can rapidly reconstruct hydrogen-bonded networks, which enables quick viscosity recovery and excellent thixotropic behavior, making it the preferred agent in high-solid-content metal pastes [22, 23]. However, the hydrogen-bond network formed by PW is generally overly rigid, leading to poor leveling after de-molding, as well as local aggregation or porosity at high silver loadings, which compromises the continuity and densification of the conductive pathways. Phase-separating polymers can form reversible microphase networks, providing structural support under low shear conditions while undergoing network reconstruction under high shear, thereby exhibiting typical shear-thinning and thixotropic behavior. For different types of phase-separating polymers, variations in microphase size, chain composition, and hard-soft segment ratio result in differences in their microstructural networks, which play a critical role in regulating the rheological performance of the system [24–27]. Block copolymers are one of the representative phase-separating polymers. They possess flexible chain segments and reversible network structures, through which they exhibit the potential to regulate thixotropic behavior in various highly dispersed systems [28, 29].

In this study, the microphase-separated styrene-ethylene-propylene-styrene block copolymer (SEPS) was introduced as a thixotropic agent to regulate the microstructure of silver pastes. SEPS forms a reversible and elastic microgel network through the cooperative interactions between its hard and soft segments, enabling dynamic interfacial modulation. The hard segments maintain the structural skeleton while interacting with the organic layer on silver particles, reinforcing interfacial adsorption and particle dispersion. This interaction mainly relies on van der Waals forces, electrostatic interactions, and hydrophobic interactions, thereby enhancing the connection between the organic carrier and the silver particles. Through this mechanism, the hard segments effectively isolate the silver particles, reducing inter-particle attraction and preventing particle aggregation or clumping. Meanwhile, the soft segments form a flexible interfacial layer that rearranges under shear to enable shear-thinning behavior and quickly restores viscoelasticity. In addition, the microstructure of the organic carrier and its interactions with silver particles were systematically examined to understand their role in flow and interface regulation. The results demonstrate that SEPS forms a reversible microgel network through the synergy of hard and soft segments, enabling dynamic modulation of the organic-inorganic interface and promoting uniform particle dispersion, while simultaneously enhancing both rheological behavior and post-sintering electrical performance.

2 | Results and Discussion

2.1 | Design and Characterization of Thixotropic Organic Carriers

Printed electronics and power devices advance toward microstructuring, high precision, and large-scale manufacturing. In this context, the dispersion, processability, and sintering densification of high-temperature conductive pastes are critical factors influencing the electrical performance and reliability of final devices. In high-solid-content silver pastes, the organic carrier not only governs the rheological behavior and printability of the paste but also directly influences the interfacial interactions of silver particles and the sintering process.

As shown in Figure 1, PW is rich in amide groups and can form a 3D homogeneous gel network with the thickening agent ethyl cellulose (EC) through reversible hydrogen bonding. Under shear, this network can be disrupted and rapidly reconstructed, exhibiting pronounced thixotropic recovery, making PW a widely used thixotropic agent. However, in high-solid-content silver pastes, the dispersion of silver particles is primarily governed by hydrogen-bond-mediated interparticle bridges, accompanied by the cooperative influence of van der Waals interactions. Hydrogen bonds originating from the amide groups in PW form particle bridges between silver particles, enhancing the structural stability and dispersion of the system, while the functional contribution of van der Waals interactions is mainly manifested between silver particles and the organic carrier molecules. Specifically, van der Waals interactions induced by instantaneous dipoles provide the fundamental driving force for the physical adsorption of organic carrier molecules on the silver particle surfaces, helping to form molecular layer spacing when particles approach each other, thereby reducing direct contact between silver particles and slowing spontaneous aggregation during storage [30–32]. Therefore, van der Waals interactions provide a fundamental contribution to the dispersion and stability of the silver paste. These forces become more significant as the silver content increases. As the performance requirements of silver particles rise (i.e., higher demands for dispersion and flowability) and processing conditions become more stringent (e.g., printing at high shear rates), these interactions cause the network to exhibit local rigidity. Specifically, at high silver content, the hydrogen bonds and van der Waals forces strengthen the connections between particles, making the paste less fluid under shear, thus

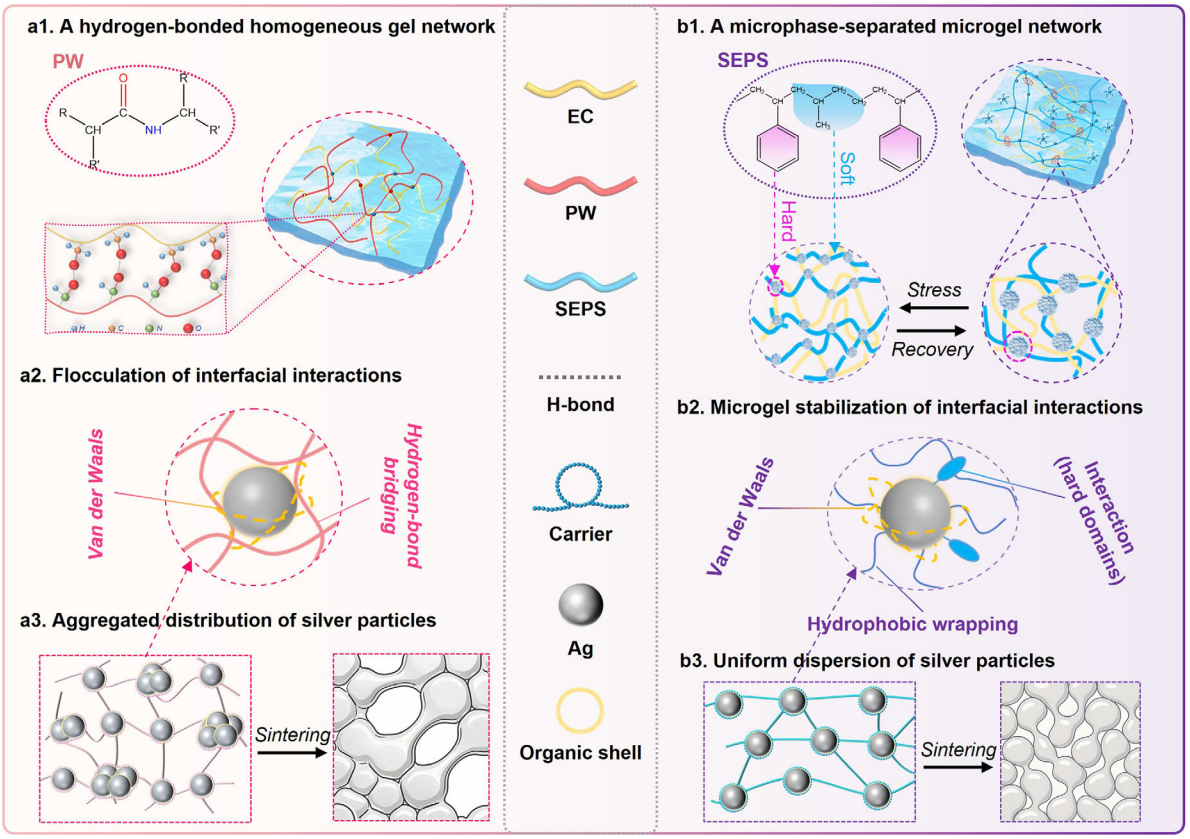

FIGURE 1 | Mechanistic illustration of silver paste regulation by two organic carrier systems. **Left**: The hydrogen-bonded homogeneous gel network of PW, formed by rigid amide chains, showing local silver aggregation and flocculation via hydrogen-bond bridging and van der Waals interactions. **Right**: The microphase-separated microgel network of SEPS, consisting of hard polystyrene (PS) segments and soft ethylene-propylene (EP) segments, enables uniform silver dispersion and stabilization through multiple interfacial interactions.

exhibiting local rigidity. This can lead to particle aggregation or flocculation, compromising print uniformity and sintering densification.

In contrast, SEPS block elastomers provide a new route for structural and functional control. SEPS consists of styrene (S) and ethylene-propylene (EP) segments, forming a microphase-separated structure with distinct hard (S) and soft (EP) domains. The hard segments aggregate to form a rigid skeleton maintaining structural integrity, while the soft segments provide flexible chains capable of stress absorption and reversible rearrangement. Based on this dual structure, SEPS can self-assemble into a microgel network in solvent. The polymer chains can reversibly disentangle and slide under external force, achieving stable and controllable thixotropic behavior. This allows SEPS to serve as a core thixotropic agent. More importantly, the hard segments reinforce the network skeleton and partially interact with the silver particles, providing local structural support, while the nonpolar soft segments interact with the particle surface via hydrophobic and van der Waals interactions. This enables uniform and long-term stable dispersion of silver particles within the microphase-separated microgel network, thereby enhancing paste printability and sintering densification.

To further elucidate the origins of their distinct thixotropic behaviors, the molecular structure and condensed states of the two thixotropic agents were characterized by differential scanning calorimetry (DSC) and Fourier transform infrared spectroscopy (FTIR). As shown in Figure S1, SEPS exhibits a glass transition at -57.4°C, indicating segmental relaxation of the ethylene-butylene soft blocks. A weak thermal event at 122.4°C suggests only limited microphase separation of the polystyrene hard blocks, consistent with its low hard-block fraction [33]. By contrast, the melting peaks observed at 48.2°C and 103.8°C in the PW indicate the presence of crystalline regions in the polyamide chains. To investigate the origin of these crystallization phenomena, we performed FTIR spectral analysis (Figure S2). The N-H stretching vibration peak near 3301 cm^{-1} in the FTIR spectrum indicates the presence of amide bonds, supporting the formation of a hydrogen-bonded network. By combining the DSC and FTIR data, we further speculate that they may facilitate the formation of crystalline structures, providing strong evidence for hydrogen-bond-mediated physical crosslinking. Additionally, gel permeation chromatography (GPC, Figure S3) measures the number-average molecular weight of the SEPS used here as Mn = 125,004.

2.2 | Structural and Molecular Features of Organic Carriers

The thixotropic agent, thickener, and other auxiliary additives were precisely weighed according to the designed proportions and mixed with the organic solvents. The mixture was then processed

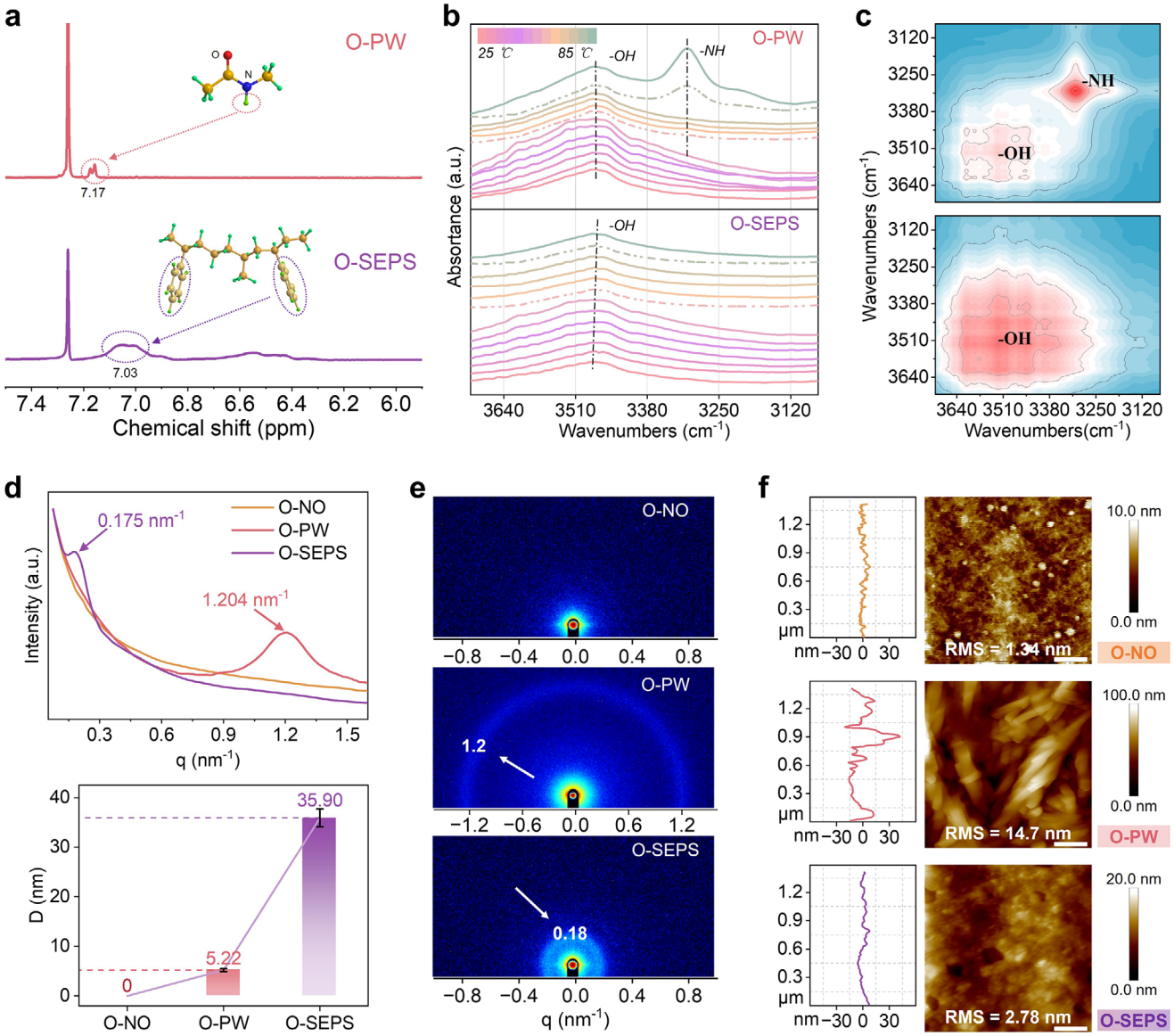

FIGURE 2 | Multiscale structural characterization of organic carriers with different thixotropic agents. (a) ^{1}H NMR spectra of the O-PW and O-SEPS; b) Variable-temperature FTIR spectra of the O-PW and O-SEPS; (c) Synchronous 2D correlation FTIR spectra corresponding to (b); (d) 1D SAXS profiles and calculated D values of the organic carriers with different thixotropic agents; (e) 2D SAXS patterns and (f) AFM height images of the organic carriers with different thixotropic agents (scale bar is 200 nm).

in a nanoscale dispersing machine to obtain a homogeneous organic carrier system. Based on the type of thixotropic agent, the resulting carrier systems were designated as O-X, corresponding to no thixotropic agent, PW, and SEPS, respectively. Detailed compositions are provided in Table S1. Subsequently, proton nuclear magnetic resonance (^{1}H NMR) and Raman spectroscopy were performed to clarify the chemical functionalities and molecular structural differences of the thixotropic agents. As shown in Figure 2a and Figure S4, the O-PW system displays characteristic N-H proton signals, while the O-SEPS system shows chemical shifts corresponding to aromatic protons. This reflects the distinct molecular heterogeneity of the carriers. Raman spectra (Figure S5) further reveal that SEPS hard segments aggregate in an ordered manner (1582, 1602, and 1666 cm^{-1}). The broad methylene band at 2852 cm^{-1} indicates the amorphous mobility of soft segments, enabling the formation of a dynamic microphase-separated network with hard-segment interacting and soft-segment plasticizing. By contrast, the O-PW system exhibits an amide peak at 1638 cm^{-1} and red-shifted, narrowed alkyl chain peaks (2873.8 and 2937.4 cm^{-1}). These features indicate a well-ordered hydrogen-bonded network.

Next, thermogravimetric (TG) and derivative thermogravimetric (DTG) analyses, together with temperature-dependent FTIR, were used to examine how the chemical functionalities influence the thermal stability and decomposition behavior of the carriers. As shown in Figure S6, mass loss below 250°C corresponds to the gradual evaporation of residual solvents, while the subsequent high-temperature region reflects decomposition of the carrier frameworks. The O-PW system exhibits a pronounced degradation peak at approximately 379°C, corresponding to the cleavage of amide backbones (C—N bonds) and associated structural units.

And the O-SEPS system shows a characteristic peak around 433°C, attributable to the decomposition of the polystyrene hard segments. This comparison indicates that the block copolymer architecture of SEPS confers enhanced thermal stability relative to PW. Despite differences in degradation mechanisms and temperature ranges, both carriers are fully oxidized upon sintering above 500°C in air. This ensures that no residual organic matter remains to compromise the electrical performance of the silver films. Temperature-dependent FTIR (25°C–85°C) further reveals their thermal response (Figure 2b). In the O-SEPS system, the O—H stretching band at 3400 cm^{-1} shows a slight blue shift, decreased intensity, and peak narrowing. This indicates only minor relaxation of the hydroxyl hydrogen-bond network. The microgel network formed by the hard and soft segments maintains structural integrity, without observable bond cleavage or molecular rearrangement. In contrast, in the O-PW system, the -NH band gradually increases above 60°C, with a slight red shift and peak broadening. This reflects local relaxation or reorganization of the amide-amide hydrogen-bond network. The 2D-COS analysis further reveals that the thermal response of the O-SEPS functional groups is more synergistic, with a more gradual rearrangement of the hydrogen-bond network, indicating better thermal tolerance and structural integrity of the hydrogen-bond network (synchronous and asynchronous spectra, Figure 2c; Figure S7).

To further elucidate how the molecular structure of thixotropic agents governs the nanoscale organization of the carriers, small-angle X-ray scattering (SAXS) was employed to analyze the microstructure of the organic carriers (Figure 2d). The O-NT system exhibited a smooth scattering profile without distinct peaks, indicating a uniform molecular chain distribution and the absence of aggregation. The O-PW system showed a scattering peak at $q = 1.204$ nm^{-1}, indicating ≈ 5 nm clustered aggregates, consistent with hydrogen-bond-driven local ordering. The O-SEPS system displayed a broad peak at $q = 0.175$ nm^{-1}, corresponding to microgel-like aggregates of approximately 36 nm. In these aggregates, hard segments were ordered while soft segments remained amorphous and mobile. These observations are further supported by the 2D SAXS images (Figure 2e), with O-SEPS and O-PW showing distinct scattering rings, whereas O-NT showed no distinct features. Overall, the aggregation patterns of the carriers are governed by their molecular structural units, such as amide bonds or hard/soft segment combinations. This results in uniform chain distribution for O-NT, hydrogen-bonded small-cluster networks for O-PW, and microgel structures with hard-segment interacting and soft-segment plasticizing in O-SEPS. Atomic force microscopy (AFM) characterization of spin-coated and vacuum-dried films offered complementary insights into surface morphology. The AFM height images (Figure 2f) showed that the O-NT film was smooth with an RMS roughness of 1.3 nm. This indicates a near-uniform distribution of polymer chains and the absence of noticeable microphase separation or crystalline domains. The O-PW film exhibited pronounced island-like and network-like roughness with an RMS of 14.7 nm. This suggests that hydrogen-bond-driven local clusters or networks aggregated on the surface and may have undergone stacking or coalescence during drying. The O-SEPS film mainly displayed a microgel-like distribution with an RMS of 2.8 nm, accompanied by several dark regions, which likely correspond to SEPS molecular self-aggregation [28]. Overall, the surface morphology of SEPS is consistent with a microphase-separated model. In this model, hard segments form ordered interacting cores, while soft segments create flexible coronas, maintaining local order and relatively low overall roughness. In addition, the three-interval thixotropy test (3ITT) of the O-SEPS indicates that it exhibits pronounced thixotropic behavior due to its distinctive microphase-separated structure (Figure S8).

2.3 | Dispersibility and Rheological Properties of Silver Pastes

To evaluate the role of different thixotropic organic carriers in high-solid-content silver pastes, these carriers were incorporated into the paste to prepare SP-NT, SP-PW, and SP-SEPS. To optimize packing density and sintering performance, two silver powders with different particle sizes were blended. Their size distributions and morphologies are shown in Figure S9. TEM observations (Figure S10) and Raman spectra (Figure S11) further confirmed the presence of organic coatings on the silver particle surfaces [34–39]. This indicates that interactions between the organic binders and silver are mainly confined to the surface layer, rather than directly involving the metallic silver.

Systematic tests were conducted to assess the dispersibility and stability of silver particles in the various thixotropic organic carriers. First, the wetting and dispersibility of silver powders with different organic carriers were assessed via contact angle measurements on pressed silver substrates, where the silver particles served solely as the substrate (Figure 3a). The contact angle decreased rapidly at the initial stage and gradually stabilized over time. With the addition of O-PW, the contact angle increased from 48.8° to 78.2°, indicating a decrease in wettability. Additionally, the slower decrease in contact angle suggests a strong interaction between the silver particles and the organic carrier, allowing for the rapid establishment of a stable dispersion state. In the O-SEPS system, the reduction in contact angle and the rate of decrease are similar to those of O-PW, indicating that the system can quickly establish a stable dispersion state. However, the final contact angle of O-SEPS is lower (64.3°), further indicating better wettability. Significantly, although the O-NT system exhibits the best wettability among the three systems, it is prone to silver particle aggregation due to the lack of a network support structure formed by thixotropic agents. This phenomenon has been confirmed through subsequent particle size distribution experiments. The temporal evolution of the contact angle is presented in Figure S12. Subsequently, to further evaluate dispersion stability, the particle size distribution of silver dispersed in diluted carriers was analyzed (Figure 3b,c). The incorporation of both thixotropic agents significantly enhanced silver particle dispersibility and suppressed aggregation. The SP-SEPS system exhibited the smallest average particle size, 2.15 μm, indicating superior dispersibility and stability. In addition, dispersed silver was drop-coated onto silicon substrates and dried at 200°C to remove solvents. The samples were then scanned to examine internal particle distribution and aggregation (Figure 3d; Figure S13). Silver powders in the SP-SEPS system exhibited the least aggregation, followed by the SP-PW system. Excessive aggregation can increase porosity and weaken internal connectivity. Porosity measurements corroborate these observations, with the SP-SEPS system showing the lowest porosity of 8.31%.

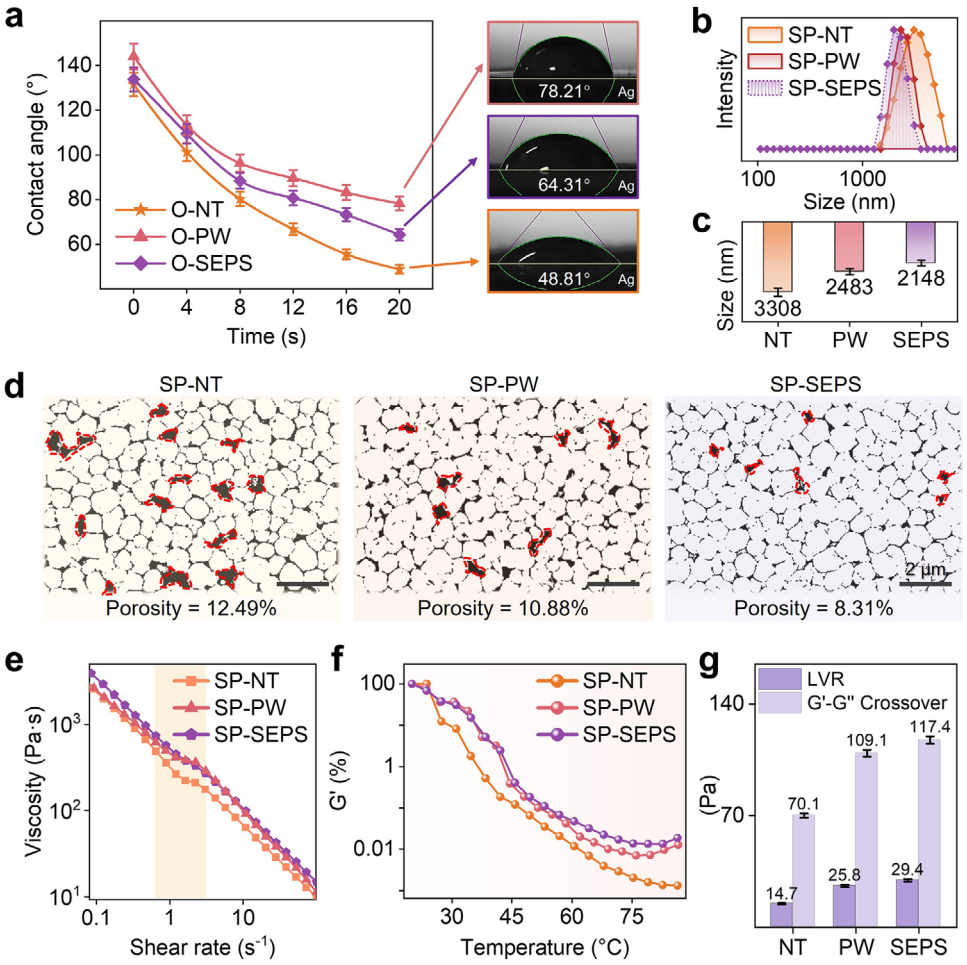

FIGURE 3 | Characterization of silver powder dispersion and silver paste rheology in organic carrier systems with different thixotropic agents. (a) Time-dependent contact angle curves of silver powders with each carrier system; (b) Particle size distribution curves and (c) Average particle size of silver powders dispersed in each carrier system; (d) SEM binary images of dried silver powders dispersed in each carrier system, showing post-drying aggregation; (e) Shear-thinning curves of silver pastes; (f) Oscillatory temperature-dependent storage modulus (G′) curves of silver pastes; (g) Relationship between storage modulus (G′), loss modulus (G″), and shear stress obtained by oscillation amplitude sweep tests for silver pastes.

In summary, the SP-SEPS system achieved the best balance of silver wetting and dispersibility, as its flexible segments uniformly covered silver surfaces, promoting orderly particle arrangement and suppressing aggregation.

Next, rheological tests were conducted to evaluate how the microstructures induced by the carriers affect the flow behavior of the silver pastes. Flow curves were analyzed using the power-law model (Equation 1), yielding two key parameters: the consistency coefficient K (reflecting viscosity at low shear rates) and the flow index n (indicating deviation from Newtonian behavior) [40, 41].

$$\eta = K \cdot \dot{\gamma}^{n-1} \tag{1}$$

The shear-thinning curves of the three silver paste samples are shown in Figure 3e. Fitting results from the power-law model are listed in Table S2. The fitting coefficients R^2 are all close to 1, indicating that the power-law model adequately describes the rheological behavior of the silver pastes. All samples exhibited $n<1$, demonstrating pronounced shear-thinning, which is critical for screen-printing applications. Among them, the SP-SEPS system displayed the highest K, ensuring stronger static support. It also exhibited a moderate n, facilitating dynamic shear response and structural recovery. Figure S14 presents the viscosity variation across different shear rates and further corroborates these performance features.

Thixotropic recovery was further assessed by a 3ITT test (Figure S15). Under simulated printing shear (100 s^{-1} for 3 s), both SP-PW and SP-SEPS systems exhibited superior structural recovery compared to the base system. This recovery ensures printability and stability during operation. Furthermore, oscillatory temperature sweep experiments were conducted to investigate the structural integrity of the pastes within a temperature range of 20°C–80°C (Figure 3f; Figure S16). The tests were performed under constant frequency (1 Hz) and small-amplitude strain conditions to ensure measurements within the linear viscoelastic region (LVR). Both the storage modulus (G′) and the viscosity decreased with increasing temperature. However, the SP-SEPS system exhibited the smallest reduction and the highest inflection point in the modulus-temperature curve, indicating enhanced network stability under thermal perturbation. This stability supports uniform dispersion and microstructural integrity during processing.

Finally, oscillatory stress sweeps (Figure 3g; Figure S17) were conducted to determine the LVR and gel point ($G' = G''$). This test is a critical approach for evaluating the structural stability and viscoelasticity of silver pastes. The LVR defines the stress range within which the sample retains its structural integrity under deformation. The results indicate that the introduction of thixotropic agents effectively extends the LVR, thereby enhancing the shear stability of the paste. The gel points of the modified systems were also shifted to higher stresses, with the SP-SEPS system exhibiting the most pronounced improvement. A higher gel point suggests that the paste can better maintain its shape and microstructure under high-stress conditions. This prevents collapse and ensures printed features with high aspect ratios. With increasing printing speed, the system may require gel point matching at higher frequencies to preserve excellent process adaptability.

2.4 | Thermal Stability and Interfacial Electronic States

Building on the rheological results, both in situ and ex situ techniques were employed to further elucidate the thermal evolution and sintering behavior of silver pastes containing different thixotropic agents. TG-DTG was performed to investigate the thermal weight loss behavior of pastes containing different thixotropic agents (Figure 4a). The TG-DTG curves can be divided into two main stages. In the first stage (<200°C), ~10 % mass loss occurred due to evaporation of volatile solvents. The second stage (200°C–400°C) involves decomposition of polymeric components, including the thixotropic agents. Within this range, the SP-SEPS exhibited higher onset and peak decomposition temperatures than the SP-PW, along with slightly greater mass loss. At 480°C, residual mass approached the theoretical silver content, indicating nearly complete removal of organic components. In situ FTIR spectra measurements were performed over the same temperature range to identify volatile species and elucidate the decomposition pathways of the organic components. Major characteristic peaks and their temperature-dependent evolution were assigned and annotated (Figure 4b,c; Figure S18). The results are consistent with the two-stage weight-loss behavior observed in the TG-DTG curves. In the low-temperature region (<200°C), the spectra were dominated by absorption bands associated with solvent evaporation. Between 200 and 480°C, multiple characteristic signals corresponding to organic decomposition products appeared. Specifically, the SP-PW exhibited an enhanced N—H absorption at 1549 cm^{-1} in the mid-temperature range. This indicates rearrangement of amide groups and the release of nitrogen-containing volatiles, accompanied by crosslinking or carbonization tendencies. In contrast, SP-SEPS showed pronounced aromatic ring fingerprints (671 cm^{-1}) and CO_2 signals (2358/2317 cm^{-1}) at higher temperatures, reflecting the cleavage of the polystyrene hard segments into aromatic fragments and small oxidized molecules. Common features for both systems included 1763 cm^{-1} (C═O), 1233 cm^{-1} (C—O), 1127/1065 cm^{-1} (C—O—C, ether/ester), and 1376 cm^{-1} (-CH_3) and 1450 cm^{-1} (-CH_2). These peaks can be used to track the decomposition sequence of various chemical bonds.

Thus, these chemical differences are expected to significantly affect silver particle sintering kinetics and densification pathways during sintering. In SP-PW, the rearrangement of amide groups and partial carbonization form crosslinked structures that restrict surface diffusion, resulting in smaller and unevenly distributed grains. In contrast, during the decomposition of SP-SEPS, low-molecular-weight aromatic fragments are generated, while the residual polymer matrix provides moderate support, promoting uniform particle necking and the formation of larger, more continuous grains.

In situ XRD measurements were further used to track the phase evolution and grain growth of SP-PW and SP-SEPS during heating from 25°C to 480°C (Figure 4d), confirming that the previously observed chemical behavior influences silver particle sintering. Characteristic metallic silver peaks were observed throughout, with no oxides or other crystalline phases detected. As temperature increased, the Ag (111) peak intensity rose while FWHM decreased, reflecting continuous grain growth and densification (Figure 4e). Scherrer-derived grain sizes reveal three stages: Stage I (<260°C) shows slow growth; Stage II (260°C–340°C) exhibits accelerated growth or minor fluctuations; Stage III (>340°C) shows continued growth approaching stabilization. The SP-PW reached an average grain size of 46.63 nm at Stage III, exhibiting minor fluctuations during Stage II. In contrast, the SP-SEPS showed rapid growth in Stage II followed by slower increase in Stage III, ultimately attaining 77.63 nm (Figure 4f, inset SEM images before and after heating). Figure S19 shows SEM images at different temperatures, further confirming the disparity in grain growth and densification between the two systems. SP-SEPS promotes more efficient sintering, resulting in larger and more uniform silver grains. In contrast, SP-PW restricts particle diffusion, slowing early-stage grain growth and affecting the densification pathway. Additionally, XPS depth profiling was performed to analyze the chemical states and electronic interactions between the silver particles and the polymer. The results show increasing $C^{\delta-}$ (283.7 eV) and $Ag^{\delta+}$ (369.0 eV) signals with sputtering depth, with the strongest interactions observed in SP-SEPS, intermediate in SP-PW, and weakest in SP-NT (Figures S20–S22) [42].

2.5 | Microstructure and Electrical Performance of Printed Electrodes

Conductivity is a critical performance indicator for printed silver pastes, as it directly determines their applicability in power devices, photovoltaic modules, and microelectronic interconnects. After infrared sintering at high temperature, the electrical resistance of the silver paste samples was measured with a micro-ohmmeter, and the volume resistivity was calculated from the measured cross-sectional area obtained by 3D optical microscopy. Each sample was tested multiple times to ensure reproducibility. Two representative test patterns were designed to reflect different application scenarios. The first pattern consists of wide lines (2 mm), representing high-power conductive applications (Figure 5a). In this case, high electrical conductivity is crucial for efficient current transport, while the relatively large line thickness allows some tolerance for porosity. The second pattern consists of fine lines (100 μm), corresponding to high-precision micro structured circuits (Figure 5b). Here, conductivity is more sensitive to sintering densification, as microvoids or uneven particle dispersion can significantly increase resistivity.

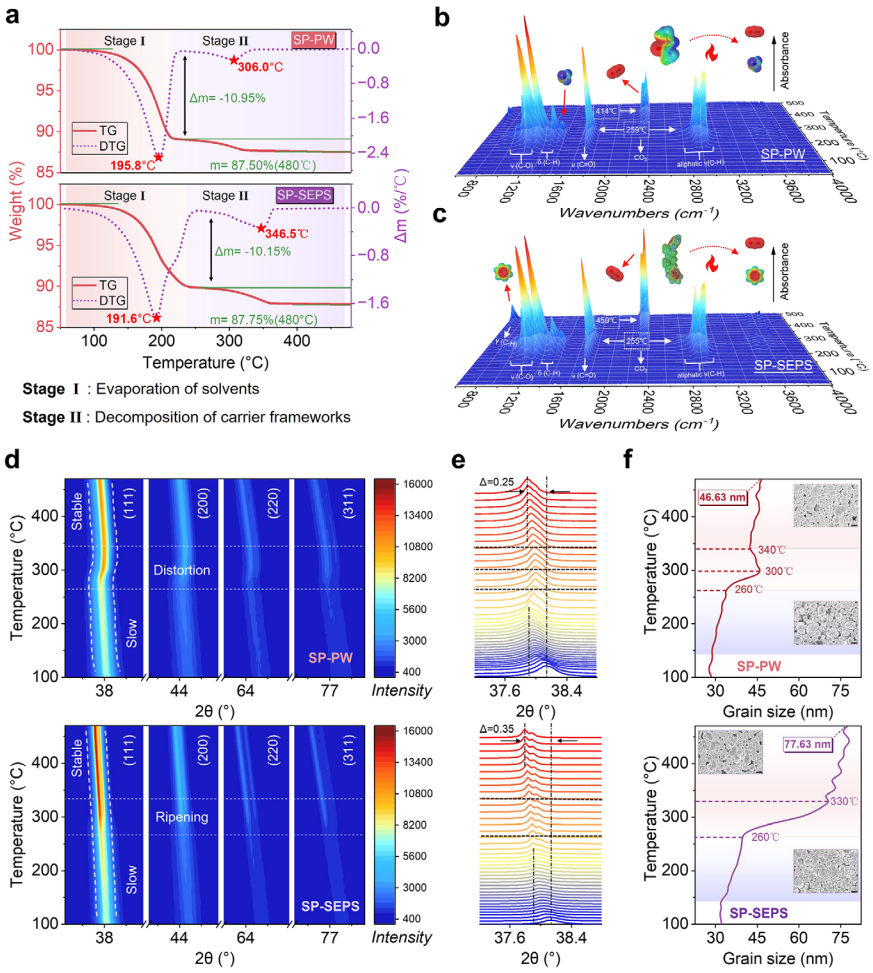

FIGURE 4 | Thermal and microstructural characterization of silver pastes prepared with organic carrier systems with different thixotropic agents. (a) TG-DTG curves of silver pastes prepared with each carrier system; (b,c) In situ FTIR spectra of silver pastes prepared with each carrier system; (d) In situ high-temperature XRD patterns and (e) XRD profiles of silver pastes with each carrier system; (f) Grain growth curves of silver powders at different temperatures, with SEM images before and after heating shown as insets (scale bar is 1 μm).

The detailed test results are summarized in Tables S3 and S4. Under the fine-line conditions, the SP-SEPS exhibited a markedly lower resistivity of 3.03 μΩ·cm, outperforming the other systems. The wide-line pattern further confirms this advantage.

Furthermore, to elucidate the origin of the improved electrical performance in the sintered electrodes, cross-sectional characterization was conducted to assess porosity (Figure 5c,d; Figure S23). 3D imaging was first employed to reveal variations in grid line height. Subsequently, multiple positions were selected at equal intervals along a 1 mm electrode, and cross-sections were prepared using FIB. The porosity was then quantified by ImageJ analysis to enable direct comparison. The results show that the SP-SEPS sample exhibited a porosity of 8.66%. This value is significantly lower than the 9.12% measured for the SP-PW sample, corresponding to a 5.1% relative reduction. Notably, the SP-SEPS sample displayed smaller and more uniformly distributed pores, and its printed line morphology was more continuous and uniform. In contrast, the SP-PW sample contained larger, irregular pores with a broader size distribution. The SP-SEPS microstructure was denser and more homogeneous, with fewer voids and enhanced silver particle connectivity. These structural features effectively improve the electrical conductivity of the printed electrode.

Next, we evaluated the practical applicability of the silver pastes by testing the printing fidelity of formulations containing different thixotropic agents. The 3D morphology of screen-printed electrodes under high-speed printing conditions was analyzed using laser confocal microscopy (Figure S24). This technique provides high-resolution 3D images of the electrode surface, allowing for precise measurement of surface roughness and high aspect ratio features, offering a clearer understanding of the morphology. Due to varying rheological properties, the printed electrode's line geometry and surface morphology also exhibited differences. All formulations displayed a certain degree of ink spreading (electrode widths > 20 μm). The results showed that the paste without a thixotropic agent exhibited severe morphological collapse and uneven surfaces due to low yield stress and poor network stability. With PW addition, the morphology became smoother and more stable. SP-SEPS achieved the best uniformity and surface smoothness, as its excellent dispersion and thixotropy maintained structural elasticity and minimized spreading. The printed characteristic dimensions were a line width of 26.61 μm, a height of 13.77 μm, and an aspect ratio of 0.517. As shown in

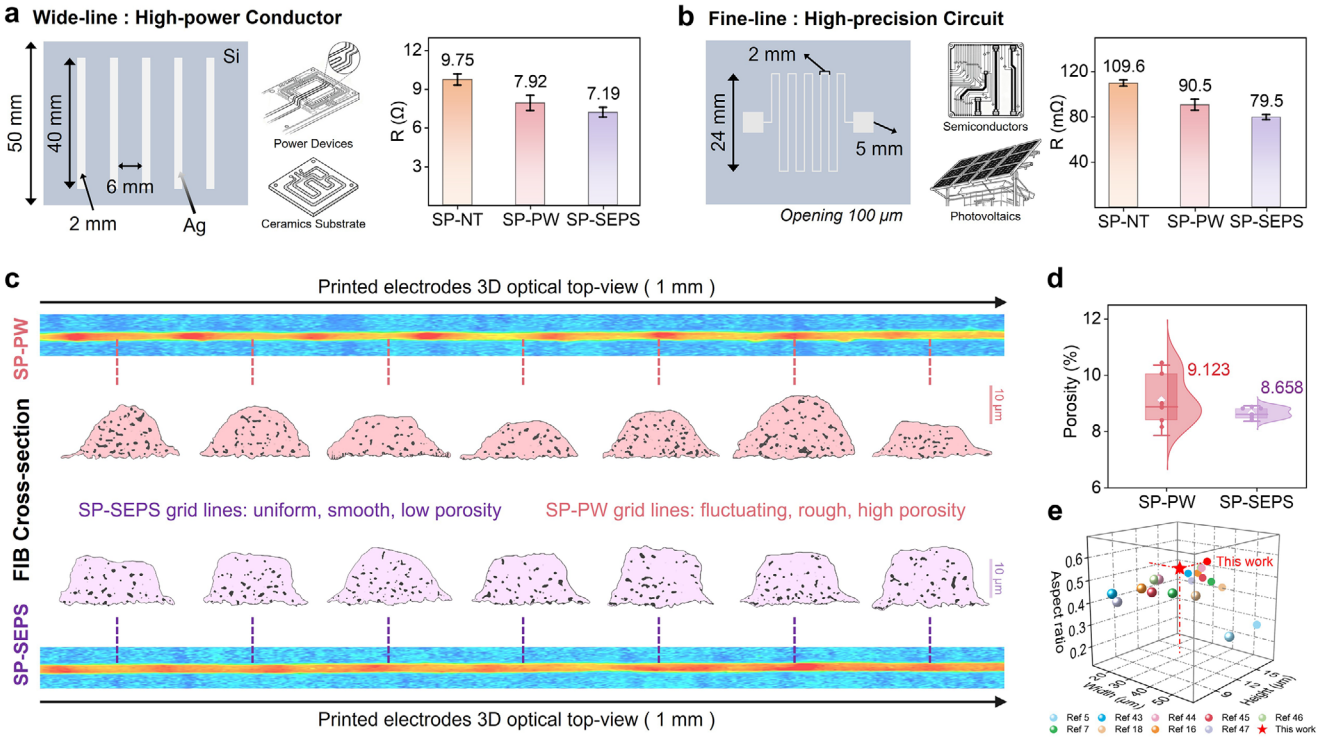

FIGURE 5 | Printed electrodes and microstructural characterization of silver pastes prepared with organic carrier systems with different thixotropic agents. (a) Wide-line electrodes and corresponding resistivity, representing high-power conductor applications; (b) Fine-line electrodes and corresponding resistivity, representing high-precision microcircuit applications; (c) 3D optical top-view and SEM cross-sectional images of sintered electrodes prepared with each system; (d) Porosity of sintered electrodes, averaged from multiple random locations; (e) Comparison of printed electrode height, width, and aspect ratio with reported literature values.

Figure 5e, these printed characteristics also demonstrate certain advantages when compared to results reported in related studies [5, 7, 16, 18, 43–47]. Overall, the SP-SEPS effectively maintains the balance between shear-thinning flowability and structural recovery, a crucial characteristic for achieving high-resolution printing.

In addition, the shrinkage rate of the electrodes before and after sintering was measured using a laser confocal microscope (Figure S25). The results show that electrodes from different thixotropic agent systems exhibit similar shrinkage behaviors, with a shrinkage rate of approximately 11%, with no significant differences observed. This indicates that the thixotropic agents have a minimal impact on the shrinkage of the silver paste and do not negatively affect the structural stability or functional performance of the electrodes. Furthermore, to evaluate the impact of different thixotropic agent systems on the adhesion between the electrode and substrate, we used the cross-cut adhesion test method to measure the adhesion of the electrodes after sintering (Figure S26). The results indicate that the electrodes prepared with all systems exhibited good adhesion, with no issues of poor adhesion observed.

3 | Conclusion

In this work, we introduce a microphase-separated SEPS elastomer as a thixotropic agent for printable conductive pastes. Unlike the conventional PW system, which relies on hydrogen-bond clusters that promote particle bridging and flocculation, the SEPS elastomer integrates rigid segments for surface interacting with flexible segments that enhance interfacial contact and dispersion. This hard-soft segment synergy forms a microphase-separated microgel network that combines structural support with dynamic responsiveness. The resulting network modifies organic-inorganic interfacial interactions, thereby improving paste printability and enhancing post-sintering conductivity. Consequently, the paste exhibits improved rheological characteristics, enabling high-speed, fine-line printing with excellent shape fidelity. Furthermore, the specific thermal behavior of SEPS segments and the staged removal of the organic phase during heating facilitate gradual particle necking and grain growth during sintering, ultimately reducing porosity. These microstructural improvements are directly translated into enhanced electrical performance, with the sintered electrodes achieving a low resistivity of 3.03 μΩ·cm. In summary, this strategy enables the synergistic enhancement of paste printability and post-sintering electrical performance. The incorporation of microphase-separated SEPS elastomers establishes a rational carrier design paradigm for high-performance electrodes in precision printed electronics and photovoltaic gridlines.

Author Contributions

Z.H.: Conceptualization, investigation, data curation, writing – original draft. H.J.: writing – review and editing. Z.Z.: Data curation. J.L.:

Conceptualization, investigation. L.Y.: Resources, writing – review and editing. Y.L.: Conceptualization, supervision, writing – review and editing. F.P.: Resources, writing – review and editing.

Acknowledgements

The author would thank the support of the Soft Science Research Project of Guangdong Province (No. 2017B030301013), and the Guangdong Innovative Team Program (No. 2013N080).

Conflicts of Interest

The authors declare no conflicts of interest.

References

1. L. Yang, H. Hu, A. Scholz, et al., "Laser Printed Microelectronics," *Nature Communications* 14 (2023): 1103.

2. H. Lin, M. Yang, X. Ru, et al., "Silicon Heterojunction Solar Cells with up to 26.81% Efficiency Achieved by Electrically Optimized Nanocrystalline-Silicon Hole Contact Layers," *Nature Energy* 8 (2023): 789–799, https://doi.org/10.1038/s41560-023-01255-2.

3. S. Tepner and A. Lorenz, "Printing Technologies for Silicon Solar Cell Metallization: A Comprehensive Review," *Progress in Photovoltaics: Research and Applications* 31: 557–590, https://doi.org/10.1002/pip.3674.

4. Y. Qin, X. Ouyang, Y. Lv, W. Liu, Q. Liu, and S. Wang, "A Review of Carbon-Based Conductive Inks and Their Printing Technologies for Integrated Circuits," *Coatings* 13 (2023): 1769.

5. G. R. Lopes, J. Jourdan, S. Bastide, and W. Favre, "Evaluation of Commercial Pure Conductive Copper Pastes by Screen Printing for a-Si: H/c-Si Heterojunction Solar Cells," *Solar Energy Materials and Solar Cells* 292 (2025): 113690.

6. C. Yuece, M. Koenig, and N. Willenbacher, "Rheology and Screen-Printing Performance of Model Silver Pastes for Metallization of Si-Solar Cells," *Coatings* 8 (2018): 406.

7. S. Zhao, K. Hu, M. Huang, et al., "Optimization of Capillary Suspension Silver Pastes for Enhanced Metallization in Silicon Solar Cells: a Comparative Analysis of Screen-Printing and Pattern Transfer Printing," *Solar Energy* 277 (2024): 112746.

8. H.-W. Lin, C.-P. Chang, W.-H. Hwu, and M.-D. Ger, "The Rheological Behaviors of Screen-Printing Pastes," *Journal of Materials Processing Technology* 197 (2008): 284–291, https://doi.org/10.1016/j.jmatprotec.2007.06.067.

9. K. Inukai, Y. Takahashi, K. Ri, and W. Shin, "Rheological Analysis of Ceramic Pastes with Ethyl Cellulose for Screen-printing," *Ceramics International* 41 (2015): 5959–5966, https://doi.org/10.1016/j.ceramint.2015.01.032.

10. D. Li, X. Liu, X. Chen, W.-Y. Lai, and W. Huang, "A Simple Strategy towards Highly Conductive Silver-Nanowire Inks for Screen-Printed Flexible Transparent Conductive Films and Wearable Energy-Storage Devices," *Advanced Materials Technologies* 4 (2019): 1900196.

11. M. Ali, L. Lin, S. Faisal, I. A. Sahito, and S. I. Ali, "Optimisation of Screen Printing Process for Functional Printing," *Pigment & Resin Technology* 48 (2019): 456–463, https://doi.org/10.1108/PRT-05-2019-0043.

12. H. J. Nam, M. Shin, H. Y. Koo, S.-H. Park, H. M. Nam, and S.-Y. Nam, "Physical Properties of Paste Synthesized from Wet-and Dry-Processed Silver Powders," *Materials* 17 (2024): 1273.

13. S. Thibert, J. Jourdan, B. Bechevet, D. Chaussy, N. Reverdy-Bruas, and D. Beneventi, "Influence of Silver Paste Rheology and Screen Parameters on the front Side Metallization of Silicon Solar Cell," *Materials Science in Semiconductor Processing* 27 (2014): 790–799, https://doi.org/10.1016/j.mssp.2014.08.023.

14. S. Thibert, J. Jourdan, B. Bechevet, et al., "Study of the High Throughput Flexographic Process for Silicon Solar Cell Metallisation," *Progress in Photovoltaics: Research and Applications* 24 (2016): 240–252, https://doi.org/10.1002/pip.2659.

15. C. Xu and N. Willenbacher, "How Rheological Properties Affect Fine-Line Screen Printing of Pastes: A Combined Rheological and High-Speed Video Imaging Study," *Journal of Coatings Technology and Research* 15 (2018): 1401–1412, https://doi.org/10.1007/s11998-018-0091-2.

16. Y. Tian, C. Mao, X. Zhou, et al., "An Optimization Strategy for Improving the Aspect Ratio of Screen Printing Electronic Paste Based on Rheological Properties," *Colloids and Surfaces a-Physicochemical and Engineering Aspects* 697 (2024): 134453.

17. C. Mao, Y. Tian, X. Zhou, J. Bai, S. Ma, and H. Wang, "Unification of Rheology of Thixotropic Yield Stress Fluids and Screen Printing Properties of Pastes," *Colloids and Surfaces a-Physicochemical and Engineering Aspects* 682 (2024): 132982.

18. Y. Tian, C. Mao, Q. Li, Z. Sun, S. Ma, and H. Wang, "How Do Organic Additives Affect the Properties of Electronic Pastes: A Combined Study of Rheology and Printability," *Journal of Materials Science-Materials in Electronics* 36 (2025): 244.

19. J.-X. Wu, C. P. Chu, and Y.-C. Liao, "Solderable Conductive Paste for Electronic Textiles," *Journal of the Taiwan Institute of Chemical Engineers* 142 (2023): 104616.

20. Y. Gao, J. Feng, F. Liu, and Z. Liu, "Effects of Organic Vehicle on the Rheological and Screen-printing Characteristics of Silver Paste for LTCC Thick Film Electrodes," *Materials* 15 (2022): 1953.

21. M. A. Kuzina, D. D. Kartsev, A. V. Stratonovich, and P. A. Levkin, "Organogels versus Hydrogels: Advantages, Challenges, and Applications," *Advanced Functional Materials* 33 (2023): 2301421.

22. Y. Hu, Y. Huang, L. Li, et al., "Preparation and Printing Optimization of an Organic Carrier for Silver Paste on the front Side of Solar Cells," *Rsc Advances* 15 (2025): 27026–27032.

23. X. Huang, X. Meng, M. Li, J. Sun, K. Lv, and C. Gao, "Improving the Weak Gel Structure of an Oil-Based Drilling Fluid by Using a Polyamide Wax," *Gels* 8 (2022): 631.

24. Z.-F. Zhao, P.-Y. Liu, C.-Q. Zhang, et al., "Synthesis and Properties of SEPS-g-PEO Copolymers with Varying Branch Lengths," *Chinese Journal of Polymer Science* 36 (2018): 934–942, https://doi.org/10.1007/s10118-018-2104-0.

25. S. O. Ilyin, "Structural Rheology in the Development and Study of Complex Polymer Materials," *Polymers* 16 (2024): 2458.

26. F. S. Bates, M. A. Hillmyer, T. P. Lodge, C. M. Bates, K. T. Delaney, and G. H. Fredrickson, "Multiblock Polymers: Panacea or Pandora's Box?," *Science* 336 (2012): 434–440, https://doi.org/10.1126/science.1215368.

27. S. Wu and Q. Chen, "Advances and New Opportunities in the Rheology of Physically and Chemically Reversible Polymers," *Macromolecules* 55 (2022): 697–714, https://doi.org/10.1021/acs.macromol.1c01605.

28. X. Zheng, X. Wu, Q. Wu, et al., "Thorough Optimization for Intrinsically Stretchable Organic Photovoltaics," *Advanced Materials* 36 (2024): 2307280.

29. K. Liu, J. Wang, X. Pan, et al., "n-Type Thermoelectric Elastomers," *Nature* 644 (2025): 920–926.

30. Y. Hirakawa, K. Aoshima, S. Arai, and T. Hasegawa, "Phase and Dispersion Stability of Silver Nanocolloids for Nanoparticle-Chemisorption Printing," *Acs Applied Nano Materials* 2 (2019): 4342–4349, https://doi.org/10.1021/acsanm.9b00795.

31. Z. Wang, D. Wang, C. Zhang, et al., "A Fluorinated Polyimide Based Nano Silver Paste with High Thermal Resistance and Outstanding Thixotropic Performance," *Polymers* 15 (2023): 1150.

32. S. Tepner, N. Wengenmeyr, M. Linse, A. Lorenz, M. Pospischil, and F. Clement, "The Link between Ag-Paste Rheology and Screen-Printed Solar Cell Metallization," *Advanced Materials Technologies* 5 (2020): 2000654.

33. J. Zhang and F. S. Bates, "Dodecagonal Quasicrystalline Morphology in a Poly(styrene- b -isoprene- b -styrene- b -ethylene oxide) Tetrablock

Terpolymer," *Journal of the American Chemical Society* 134 (2012): 7636–7639, https://doi.org/10.1021/ja301770v.

34. R. Jiang, B. Li, C. Fang, and J. Wang, "Metal/Semiconductor Hybrid Nanostructures for Plasmon-Enhanced Applications," *Advanced Materials* 26 (2014): 5274–5309, https://doi.org/10.1002/adma.201400203.

35. L. Yin, F. Yang, X. Bao, et al., "Low-Temperature Sintering of Ag Nanoparticles for High-Performance Thermoelectric Module Design," *Nature Energy* 8 (2023): 665–674, https://doi.org/10.1038/s41560-023-01245-4.

36. M. Li, Y. Xiao, Z. Zhang, and J. Yu, "Bimodal Sintered Silver Nanoparticle Paste with Ultrahigh Thermal Conductivity and Shear Strength for High Temperature Thermal Interface Material Applications," *Acs Applied Materials & Interfaces* 7 (2015): 9157–9168, https://doi.org/10.1021/acsami.5b01341.

37. D. W. Boukhvalov, I. S. Zhidkov, E. Z. Kurmaev, E. Fazio, S. O. Cholakh, and L. D'Urso, "Atomic and Electronic Structures of Stable Linear Carbon Chains on Ag-Nanoparticles," *Carbon* 128 (2018): 296–301, https://doi.org/10.1016/j.carbon.2017.11.044.

38. Y. Li, Z. Chen, R. Zhou, et al., "Design of Advanced Porous Silver Powder with High-Sintering Activity to Improve Silicon Solar Cells," *Nano Research* 17 (2024): 3189–3197, https://doi.org/10.1007/s12274-023-6163-3.

39. A. Hu, J. Y. Guo, H. Alarifi, et al., "Low Temperature Sintering of Ag Nanoparticles for Flexible Electronics Packaging," *Applied Physics Letters* 97 (2010): 153117.

40. H. Song, X. Wang, W. Xie, Z. Di, and F. Cheng, "Effect of Rheological Additives on Rheological Properties of Fly Ash-based Sealing Coatings," *Construction and Building Materials* 326 (2022): 126734.

41. S. Bilal, "Analysis about Impact of Morphological and Nanoparticle Volume Fraction Aspects of TiO_2–Cu in Enhancement of Thermophysical Features of Newtonian Fluid Flowing in a Rotating Porous Channel," *Applied Nanoscience* 13 (2021): 405–419.

42. X. Deng, D. Alfonso, T.-D. Nguyen-Phan, and D. R. Kauffman, "Breaking the Limit of Size-Dependent CO_2 RR Selectivity in Silver Nanoparticle Electrocatalysts through Electronic Metal–Carbon Interactions," *Acs Catalysis* 13 (2023): 15301–15309, https://doi.org/10.1021/acscatal.3c03446.

43. S. Wang, H. Liu, Y. Ao, K. Okamoto, and J. Di, "Strengthening TOPCon Solar Cell Reliability via Al/Ga/Fe-Added Glass Frits in LECO-compatible Silver Pastes against Acid Corrosion," *Solar Energy Materials and Solar Cells* 292 (2025): 113776.

44. M. Ailinger, K. A. Aal, and N. Willenbacher, "Rheology and Fine-Line Screen Printing of Solar Cell Front-Side Metallization Pastes–What Really Matters," *Solar Energy Materials and Solar Cells* 292 (2025): 113763.

45. Y. Tian, S. Yu, W. Sun, S. Ma, and H. Wang, "Preparation of Electronic Pastes for High-Precision Screen Printing: Action Mechanisms and Synergistic Effects of Different Polymer Binders," *Surfaces and Interfaces* 65 (2025): 106525.

46. Y. Zhang, S. Wang, L. Wang, et al., "Silver-Lean Screen-Printing Metallisation for Industrial TOPCon Solar Cells: Enabling an 80% Reduction in Silver Consumption," *Solar Energy Materials and Solar Cells* 288 (2025): 113654.

47. N. Chen, Y. Liu, Y. Shao, et al., "Review of the Latest Industrial Progress in Screen Printing," *Solar Energy Materials and Solar Cells* 290 (2025): 113734.

Supporting Information

Additional supporting information can be found online in the Supporting Information section.

Supporting File: adma72777-sup-0001-SuppMat.docx.